Design and optimization of simulated light delivery systems for photoacoustic assessment of peripheral nerve injury

Graham, Michelle, von Guionneau, Nicholas, Tuffaha, Sami, Lediju Bell, Muyinatu

Michelle T. Graham, Nicholas von Guionneau, Sami Tuffaha, Muyinatu A. Lediju Bell, "Design and optimization of simulated light delivery systems for photoacoustic assessment of peripheral nerve injury," Proc. SPIE 11960, Photons Plus Ultrasound: Imaging and Sensing 2022, 1196012 (3 March 2022); doi: 10.1117/12.2610511

SPIE.

Event: SPIE BiOS, 2022, San Francisco, California, United States

Design and optimization of simulated light delivery systems for photoacoustic assessment of peripheral nerve injury

Michelle T. Graham[a], Nicholas von Guionneau[b], Sami Tuffaha[b], and Muyinatu A. Lediju Bell[a,c,d]

[a]Department of Electrical and Computer Engineering, Johns Hopkins University, Baltimore, MD, USA
[b]Department of Plastic and Reconstructive Surgery, Johns Hopkins University School of Medicine, Baltimore, MD, USA
[c]Department of Biomedical Engineering, Johns Hopkins University, Baltimore, MD, USA
[d]Department of Computer Science, Johns Hopkins University, Baltimore, MD, USA

ABSTRACT

Precise assessment of nerve injury site and extent is key to optimizing outcomes after surgical nerve repair. Photoacoustic imaging is a promising technique to intraoperatively assess nerve injury. However, this imaging technique is challenged by optical scattering, which reduces light penetration into nerve tissue. This work investigates custom light delivery methods to enhance optical penetration into nerve tissue. Monte Carlo simulations were first performed with light sources operating independently at multiple wavelengths to determine an optimal wavelength of 1690 nm for light transmission, based on the rate of fluence decay, measured as a function of depth. Four configurations of simulated light sources were then investigated. For each configuration, the nerve was illuminated with sparse activation patterns that were either evenly distributed or clustered. The percent area of illuminated nerve was maximized (28.4-100%) with a 230° mixed trajectory arc, consisting of 180° radial and 50° lateral trajectories. These results indicate that a custom light delivery system with combined radial and lateral trajectory illumination will maximize optical penetration into nerve tissue for intraoperative photoacoustic assessment of nerve injury to improve reconstructive surgery outcomes.

1. INTRODUCTION

Peripheral nerve injury affects approximately 1.6-5.1% of limb trauma patients worldwide, the majority of which are caused by motor vehicle accidents.[1–5] Patients with peripheral nerve injury suffer from motor dysfunction, sensory dysfunction, decreased dexterity, pain, and varying degrees of long-term disability.[6–10] Surgical reconstructive procedures, such as direct repair (e.g., end-to-end, epineurial sleeve, end-to-side), nerve conduit repair, or nerve grafting (e.g., autografts, allografts), are necessary to restore nerve function in cases of severe peripheral nerve injury. The assessment of nerve injury (e.g., location of injury, mechanism of injury, degree of nerve transection, length of nerve gap) is a key factor that optimizes surgical reconstructive techniques and functional outcomes of the repair.[6,7,11]

Current intraoperative approaches to nerve assessment include manual palpation, electromyography, ultrasound imaging, magnetic resonance imaging, and diffusion tensor imaging. However, manual palpation is highly subjective as well as unreliable when operating on damaged tissues that differ from the normal neuroanatomy surgeons are trained to recognize. While electromyography, the monitoring of skeletal muscle electrical activity, is used as an indicator of nerve health, it is susceptible to false positives and negatives (e.g., an injured nerve may still emit a response for up to 3 days after injury despite a complete tear or an uninjured nerve may temporarily misfunction until ischemia recedes).[12,13] Similarly, ultrasound imaging provides insufficient soft tissue contrast to differentiate healthy and unhealthly nerve tissue as well as is highly operator dependent.[7,14] Although magnetic resonance imaging and diffusion tensor imaging provide superior soft tissue contrast, the tradeoff between resolution and field of view makes these modalities impractical for scanning along a nerve to identify injury. These limitations lead to suboptimal surgical decisions and 30% of patients who undergo reconstructive surgery live with permanent disability postoperatively.[15]

Photons Plus Ultrasound: Imaging and Sensing 2022, edited by Alexander A. Oraevsky, Lihong V. Wang
Proc. of SPIE Vol. 11960, 1196012 · © 2022 SPIE · 1605-7422 · doi: 10.1117/12.2610511

Photoacoustic imaging is a promising alternative intraoperative technique for the visualization and assessment of nerve tissue.[16–21] In this technique, endogenous chromophores selectively absorb pulsed light based on their inherent optical properties. The absorbed optical energy is converted to acoustic energy, and an ultrasound transducer receives the resulting signals.[22] Photoacoustic imaging of nerves relies on excitation of the lipids within the myelin sheaths of nerves. Specifically, nerves consists of axons, each wrapped in an insulating myelin sheath, bundled together by collagenous connective tissue.[6] In severe peripheral nerve injury, this internal structure is compromised, including the myelin sheath.

The potential to assess peripheral nerve injury can be realized with photoacoustic imaging by tuning the wavelength of pulsed laser light to preferentially excite the lipids with the myelin sheath. The resulting photoacoustic signal can be used as an indicator of myelin integrity and ultimately assessment of nerve injury. Despite this promise, photoacoustic imaging is challenged by optical scattering which reduces the light penetration into the nerve tissue and ultimately degrades photoacoustic signal quality.[22] Therefore, we are developing a custom light delivery method for an intraoperative nerve photoacoustic imaging system which optimizes light penetration into nerve tissue. This work compares potential excitation wavelengths, illumination configurations, and sparsity of light sources using Monte Carlo[23] simulations.

2. METHODS

Monte Carlo simulations[23,28,29] were performed with a resolution cell of 2 μm and with the approximate optical properties of peripheral nerves summarized in Table 1. Specifically, the peripheral nerve was modeled as a matrix of 6 μm diameter axons, each coated in a 2 μm thick myelin sheath and embedded within a scaffold of collagen. The outer 0.5 mm of the peripheral nerve model contained only collagen to represent the epineurium that encases peripheral nerves.[30] The background medium surrounding the nerve was modeled as air.

Two sets of simulations, were performed with the parameters summarized in Table 2. The purpose of Simulation Set 1 was to compare the optical penetration achievable with different possible wavelengths for exciting the lipids in nerve tissue. Wavelengths 1210, 1320, 1408, 1600, and 1690 nm were selected and simulated independently because these wavelengths correspond to peaks and minimums in the triacylglycerol lipid optical absorption spectrum.[25,31] The light source was a 3 mm linear array which launched photons in the trajectory described by the directional cosine $(u_x, u_y, u_z) = (0,0,1)$ where u_x, u_y, and u_z are the projection of the vector onto the x-, y-, and z- axis, respectively, as shown in Fig. 1.[28] The geometry of the peripheral nerve model was

Table 1. Simulated tissue optical properties where μ_a is optical absorption coefficient, μ_s is optical scattering coefficient, and g is the ansiotropy factor. Myelin and axon μ_s are not explicitly known and were therefore estimated based on the Mie scattering component of Eq. 2 in Ref. 22. Axon μ_a is also not explicitly known and was therefore set as a constant across wavelengths with a value of the mean of the accepted 0.1 to 10 cm^{-1} range of μ_a for biological tissues. The air background has negligible μ_a and μ_s and the anisotropy factor was 0.0, indicative of Rayleigh scattering.

Optical Property	Wavelength (nm)	Collagen	Myelin	Axon	Background
μ_a (cm^{-1})	1210	0.30[24]	1.87[25]	5.00[26]	0.05
	1320	0.19[24]	0.11[25]	5.00[26]	0.05
	1408	1.26[24]	1.24[25]	5.00[26]	0.05
	1600	1.16[24]	0.22[25]	5.00[26]	0.05
	1690	2.32[24]	4.30[25]	5.00[26]	0.05
μ_s (cm^{-1})	1210	221.98[24]	130.01[27]	78.83[27]	1.0
	1320	259.03[24]	125.06[27]	66.23[27]	1.0
	1408	182.82[24]	121.50[27]	61.73[27]	1.0
	1600	145.24[24]	114.75[27]	53.69[27]	1.0
	1690	75.18[24]	111.98[27]	50.58[27]	1.0
g	n/a	0.9[26]	0.9[26]	0.9[26]	0.0

Table 2. Monte Carlo simulation parameters.

	Simulation Set 1	**Simulation Set 2**
Grid Resolution (m)	2e-6	2e-6
Phantom Dimensions (m)	5e-3 x 5e-3	3e-3 x 3e-3
Myelin Thickness (m)	2e-6	2e-6
Axon Diameter (m)	6e-6	6e-6
Nerve Geometry	planar	circular
Wavelengths (nm)	1210, 1320, 1408, 1600,1690	1320
Number Photons	1,470,000	200,000

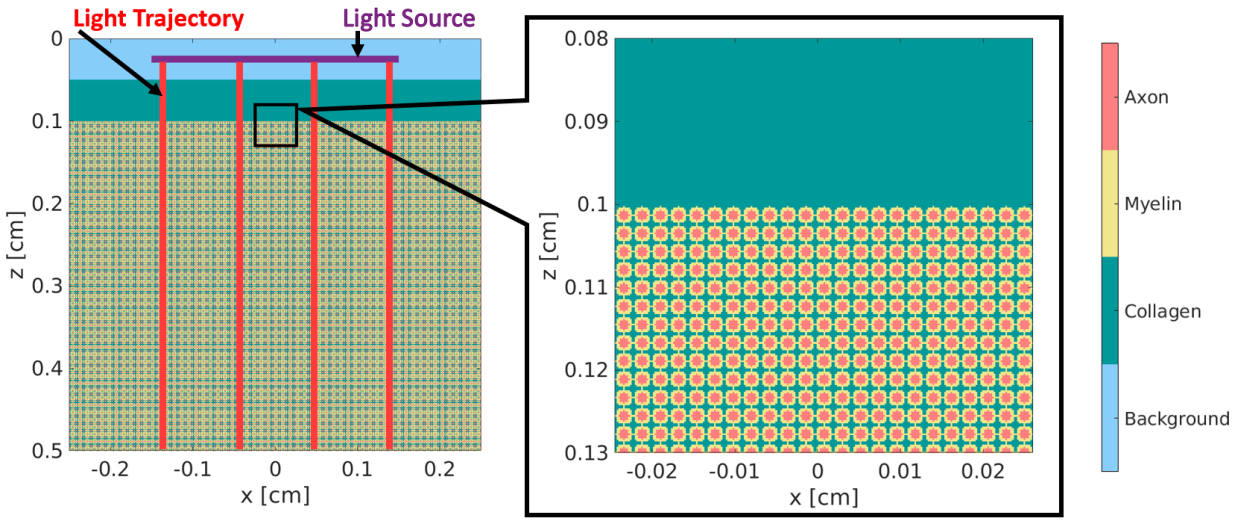

Figure 1. Set-up of the planar nerve model for simulation set 1. The light source was a 3 mm linear array with light trajectory described by the directional cosine $(u_x, u_y, u_z) = (0, 0, 1)$ and represented by the vertical red lines. The magnified section of the image demonstrates the internal nerve structure modeled as a matrix of 6 μm diameter axons, each coated in a 2 μm thick myelin sheath and embedded within a scaffold of collagen.

planar, as shown in Fig. 1. The mean fluence ± one standard deviation was measured as a function of depth, z. An exponential function, $y(z)$, was fit to the fluence and was defined as:

$$y(z) = ae^{-bz} \tag{1}$$

where a is the y-intercept and b is the rate of decay. The wavelength with the greatest rate of decay was considered to yield the poorest optical penetration.

The purpose of Simulation Set 2 was to determine the optimal light source configuration for maximum penetration of light into the peripheral nerve model. The geometry of the peripheral nerve model was circular, as shown in Fig. 2. The optimizations of Simulation Set 2 were executed for the worst case scenario, i.e., with 1320 nm wavelength light, determined as the wavelength light with the poorest optical penetration from Simulation Set 1. Optical point sources were positioned in four configurations surrounding the nerve and launched photons for four radial light trajectories including: (1) full ring; (2) 230 ° arc (representing reduced illumination due to the placement of an ultrasound probe); (3) 52° arc (representing a single source such as a fiber bundle); and (4) 230° mixed trajectory arc consisting of combined 180° radial and 50° lateral trajectories. Fig. 2 shows examples of these trajectories. With these source configurations, sparse illumination patterns included: (1) evenly distributed and (2) clustered. For the clustered activation pattern, a set number (i.e., 2 to 16) of clusters were evenly distributed along the arc and were grown in size symmetrically from the cluster centroid. The nerve area receiving $\geq$ 4.2e5 W/cm^2 fluence was measured as a function of percentage of the light sources activated

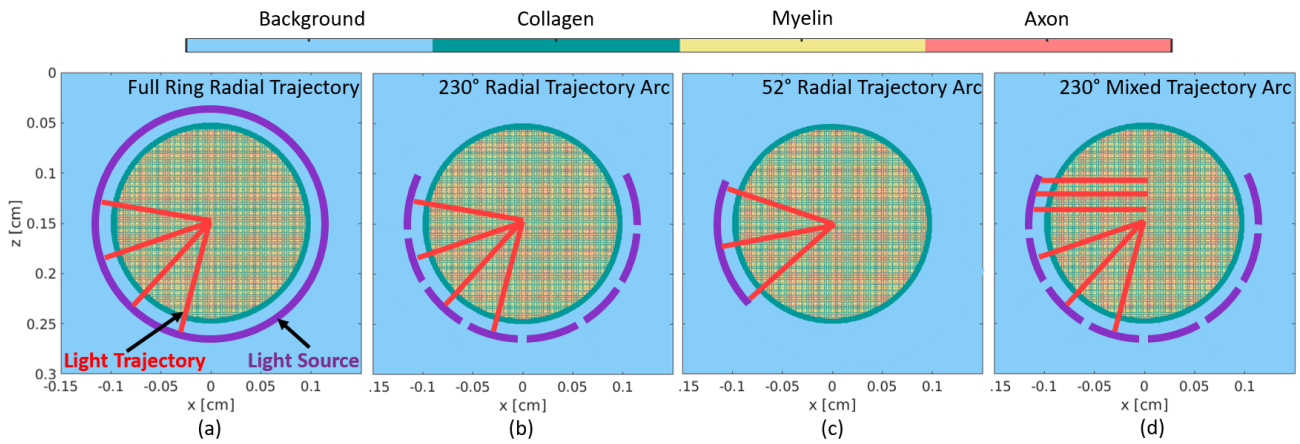

Figure 2. Set-up of circular nerve model for Simulation Set 2 including (a) full ring radial trajectory; (b) 230° radial trajectory arc (representing reduced illumination due to the placement of an ultrasound probe); (c) 52° radial trajectory arc (representing a single source such as a fiber bundle); and (d) 230° mixed trajectory arc consisting of 180° radial and 50° lateral trajectories. The red lines show a representative fraction of the radial and lateral light trajectories. (b,d) The 8 cluster illumination pattern is demonstrated.

and as a function of penetration depth. Penetration depth was categorized into superficial (i.e., outer 0.3 mm of tissue), middle (i.e., between 0.3 and 0.6 mm of tissue), and deep (i.e., $>$ 0.6 mm of tissue).

3. RESULTS

Fig. 3 shows the mean $\pm$ one standard deviation fluence decay as a function of depth for Simulation Set 1. For each wavelength simulation, fluence decays approximately as an exponential function described by Eq. 1. The legend in Fig. 3 lists the parameters of the exponential fit for each simulation. The simulation with 1320 nm light has the fastest rate of decay, $b = 163.0$, while the simulation with 1690 nm light has the slowest rate of decay, $b = 64.3$. In addition, the rate of decay corresponds to the magnitude of the wavelength-dependent collagen scattering coefficients, listed in Table 1, where $\mu_s(1320\text{ nm}) = 259.03\text{ cm}^{-1}$ is greater than $\mu_s(1690\text{ nm}) = 75.18\text{cm}^{-1}$. Therefore, 1320 nm wavelength light was considered to yield the poorest optical penetration. In order to optimize light penetration even in the worst case scenario, 1320 nm wavelength light was selected for the optimization of light delivery design in Simulation Set 2.

Fig. 4 shows the percent area of the nerve illuminated as a function of percent arc active for Simulation Set 2. The percent area of the nerve illuminated with a 52° arc was limited to 21.9%, 12.8%, and 0% for the superficial, middle, and deep nerve, respectively. The 230° radial trajectory arc and 230° mixed trajectory arc illuminations increased the percent area of the nerve illuminated to 93.2% and 100%, respectively, for the superficial nerve, 100% and 94.3%, respectively, for the middle nerve, and 100% and 40.0%, respectively, for the

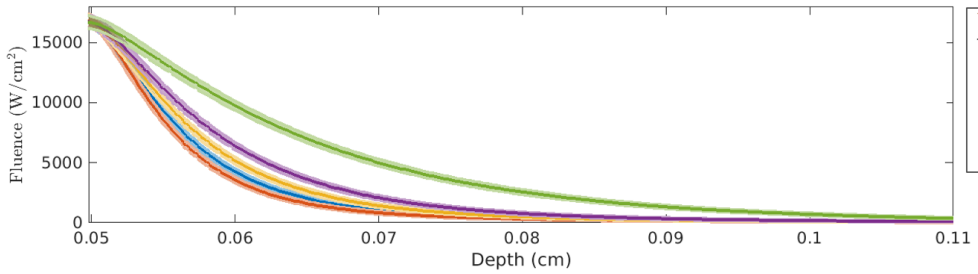

Figure 3. Mean $\pm$ one standard deviation of the fluence measured as a function of depth for each simulation in Simulation Set 1. The legend indicates the wavelengths and the associated parameters of the exponential fit described by Eq. 1 (not shown).

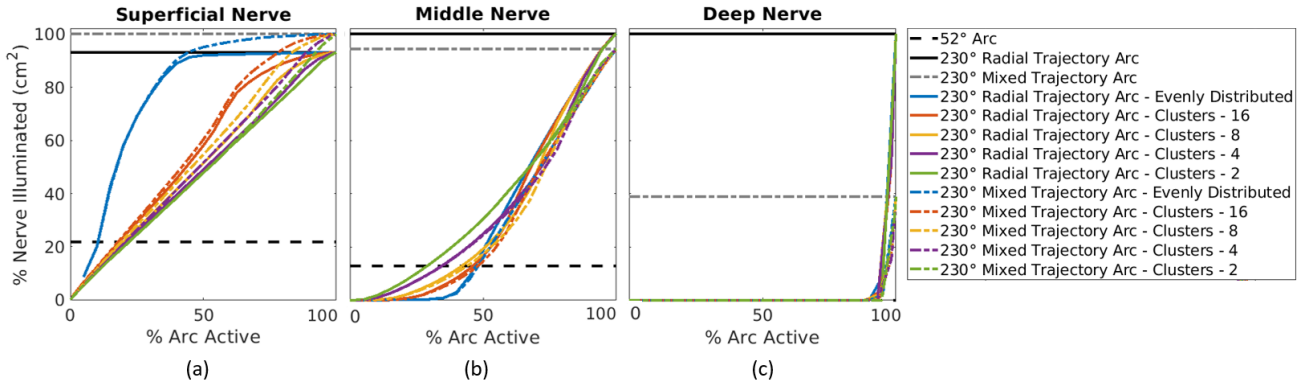

Figure 4. Percent area of the (a) superficial, (b) middle, and (c) deep nerve illuminated as a function of the percentage of the light sources activated within simulated arc. Horizontal lines represent the maximum possible percent area of the nerve illuminated for the 52° arc, 230° radial trajectory arc, and 230° mixed trajectory arc. Note that the measurements converge to the maximum possible percentage of the nerve illuminated when 100% of the light sources within the arc are activated.

deep nerve. The 230° mixed trajectory arc illumination achieved a 6.8% greater illumination of the superficial nerve whereas the 230° radial trajectory arc illumination achieved a 5.7% and 60.0% greater illumination of the middle and deep nerve, respectively. Fig. 4 also shows that, in comparing the activation patterns, the evenly distributed activation pattern enables up to 49.9% greater illumination than the cluster pattern when using sparse activation (i.e., 5-98% of the arc activated) to illuminate the superficial nerve. However, the cluster pattern with two clusters enabled up to 19.8% greater illumination than other activation patterns when using sparse activation (i.e., 5-65% of the arc activated) to illuminate the middle nerve.

4. DISCUSSION

This paper describes our investigations of a light delivery system for maximum optical penetration into peripheral nerves using Monte Carlo simulations. Both the effect of light wavelength and light source configuration on optical penetration were explored. The results of Simulation Set 1 demonstrate that light penetration into nerve tissue is dominated by the wavelength-dependent scattering coefficient of collagen (Table 1 and Fig. 3). Therefore, the excitation wavelength for photoacoustic imaging of nerves should be tuned to minimize the scattering effects of collagen.

The results of Simulation Set 2 demonstrate the potential to improve the delivery and penetration of light to and within nerve tissue when using customized illumination configurations. The 230° mixed trajectory arc and 230° radial trajectory arc configurations are preferable over typical 52° arc illumination for maximizing light penetration of the superficial and middle/deep nerve, respectively (Fig. 4). A custom light delivery system could be defined using an arc with modifiable sections for combined radial and lateral trajectory illumination. Although the optimization in Simulation Set 2 was executed for the poorest penetrating light (i.e., 1320 nm), tuning the excitation wavelength to a wavelength which minimizes optical scatter (i.e., 1690 nm), can further improve light penetration for photoacoustic imaging (Fig. 3). Furthermore, the use of two nerve geometries in the work presented in this paper demonstrates the utility of Monte Carlo simulations in designing light delivery systems for photoacoustic imaging of nerves which are optimized for a variety nerve geometries (e.g., nerves with varying epineurium or myelin thickness, axon diameter, or shape). Examples in this work demonstrated a planar geometry (representing the flattened band anatomy characteristic of either large nerve trunks or nerves compressed by inflammation[32,33]) and a circular geometry (representing a cross section from an uncompressed small- or medium-sized nerve). Future work includes building this optimal design, first *in silico* with ray tracing software and subsequently in practice with optical hardware.

5. CONCLUSION

This paper presents novel *in silico* light delivery system designs for photoacoustic imaging of nerve tissue. Simulation results demonstrate that 1320 nm and 1690 nm light are the poorest and best penetrating light,

respectively, for peripheral nerve tissue. Simulations also demonstrate that both radial and mixed trajectory illumination are required to maximize optical penetration throughout the entire circular structure of the nerve. A customized light delivery system based on these findings is expected to improve photoacoustic image quality, thereby improving the potential accuracy of photoacoustic assessments of nerve injury and the associated success rate of peripheral nerve repair surgery.

ACKNOWLEDGMENTS

This work was supported by NSF SCH Award IIS-2014088 and the NSF Graduate Research Fellowship Program (Grant No. DEG1746891).

REFERENCES

[1] Padovano, W. M., Dengler, J., Patterson, M. M., Yee, A., Snyder-Warwick, A. K., Wood, M. D., Moore, A. M., and Mackinnon, S. E., "Incidence of nerve injury after extremity trauma in the united states," *Hand* , 1558944720963895 (2020).

[2] Huckhagel, T., Nüchtern, J., Regelsberger, J., Gelderblom, M., and Lefering, R., "Nerve trauma of the lower extremity: evaluation of 60,422 leg injured patients from the TraumaRegister DGU® between 2002 and 2015," *Scandinavian Journal of Trauma, Resuscitation and Emergency Medicine* **26**(1), 1–8 (2018).

[3] Huckhagel, T., Nüchtern, J., Regelsberger, J., and Lefering, R., "Nerve injury in severe trauma with upper extremity involvement: evaluation of 49,382 patients from the TraumaRegister DGU® between 2002 and 2015," *Scandinavian Journal of Trauma, Resuscitation and Emergency Medicine* **26**(1), 1–8 (2018).

[4] Noble, J., Munro, C. A., Prasad, V. S., and Midha, R., "Analysis of upper and lower extremity peripheral nerve injuries in a population of patients with multiple injuries," *Journal of Trauma and Acute Care Surgery* **45**(1), 116–122 (1998).

[5] Taylor, C. A., Braza, D., Rice, J. B., and Dillingham, T., "The incidence of peripheral nerve injury in extremity trauma," *American Journal of Physical Medicine & Rehabilitation* **87**(5), 381–385 (2008).

[6] Siemionow, M. and Brzezicki, G., "Current techniques and concepts in peripheral nerve repair," *International Review of Neurobiology* **87**, 141–172 (2009).

[7] Rangavajla, G., Mokarram, N., Masoodzadehgan, N., Pai, S. B., and Bellamkonda, R. V., "Noninvasive imaging of peripheral nerves," *Cells Tissues Organs* **200**(1), 69–77 (2014).

[8] Novak, C. B., Anastakis, D. J., Beaton, D. E., Mackinnon, S. E., and Katz, J., "Relationships among pain disability, pain intensity, illness intrusiveness, and upper extremity disability in patients with traumatic peripheral nerve injury," *The Journal of Hand Surgery* **35**(10), 1633–1639 (2010).

[9] Ahmed-Labib, M., Golan, J. D., and Jacques, L., "Functional outcome of brachial plexus reconstruction after trauma," *Neurosurgery* **61**(5), 1016–1023 (2007).

[10] Ciaramitaro, P., Mondelli, M., Logullo, F., Grimaldi, S., Battiston, B., Sard, A., Scarinzi, C., Migliaretti, G., Faccani, G., Cocito, D., et al., "Traumatic peripheral nerve injuries: epidemiological findings, neuropathic pain and quality of life in 158 patients," *Journal of the Peripheral Nervous System* **15**(2), 120–127 (2010).

[11] Griffin, J. W., Hogan, M. V., Chhabra, A. B., and Deal, D. N., "Peripheral nerve repair and reconstruction," *Journal of Bone and Joint Surgery* **95**(23), 2144–2151 (2013).

[12] Holland, N. R., "Intraoperative electromyography," *Journal of Clinical Neurophysiology* **19**(5), 444–453 (2002).

[13] Simon, N. G., Spinner, R. J., Kline, D. G., and Kliot, M., "Advances in the neurological and neurosurgical management of peripheral nerve trauma," *Journal of Neurology, Neurosurgery & Psychiatry* **87**(2), 198–208 (2016).

[14] Luzhansky, I. D., Sudlow, L. C., Brogan, D. M., Wood, M. D., and Berezin, M. Y., "Imaging in the repair of peripheral nerve injury," *Nanomedicine* **14**(20), 2659–2677 (2019).

[15] Bergmeister, K. D., Große-Hartlage, L., Daeschler, S. C., Rhodius, P., Böcker, A., Beyersdorff, M., Kern, A. O., Kneser, U., and Harhaus, L., "Acute and long-term costs of 268 peripheral nerve injuries in the upper extremity," *PLoS One* **15**(4), e0229530 (2020).

[16] Matthews, T. P., Zhang, C., Yao, D.-K., Maslov, K. I., and Wang, L. V., "Label-free photoacoustic microscopy of peripheral nerves," *Journal of Biomedical Optics* **19**(1), 016004 (2014).

[17] Mari, J. M., Xia, W., West, S. J., and Desjardins, A. E., "Interventional multispectral photoacoustic imaging with a clinical ultrasound probe for discriminating nerves and tendons: an ex vivo pilot study," *Journal of Biomedical Optics* **20**(11), 110503 (2015).

[18] Wu, W., Wang, P., Cheng, J.-X., and Xu, X.-M., "Assessment of white matter loss using bond-selective photoacoustic imaging in a rat model of contusive spinal cord injury," *Journal of Neurotrauma* **31**(24), 1998–2002 (2014).

[19] Graham, M. T., Guo, J. Y., and Bell, M. A. L., "Simultaneous visualization of nerves and blood vessels with multispectral photoacoustic imaging for intraoperative guidance of neurosurgeries," in [*Advanced Biomedical and Clinical Diagnostic and Surgical Guidance Systems XVII*], **10868**, 108680R, International Society for Optics and Photonics (2019).

[20] Wiacek, A. and Bell, M. A. L., "Photoacoustic-guided surgery from head to toe," *Biomedical Optics Express* **12**(4), 2079–2117 (2021).

[21] Lediju Bell, M. A., "Photoacoustic imaging for surgical guidance: Principles, applications, and outlook," *Journal of Applied Physics* **128**(6), 060904 (2020).

[22] Beard, P., "Biomedical photoacoustic imaging," *Interface Focus* **1**(4), 602–631 (2011).

[23] Jacques, S. L., "Coupling 3d monte carlo light transport in optically heterogeneous tissues to photoacoustic signal generation," *Photoacoustics* **2**(4), 137–142 (2014).

[24] Sekar, S. K. V., Bargigia, I., Dalla Mora, A., Taroni, P., Ruggeri, A., Tosi, A., Pifferi, A., and Farina, A., "Diffuse optical characterization of collagen absorption from 500 to 1700 nm," *Journal of Biomedical Optics* **22**(1), 015006 (2017).

[25] Anderson, R. R., Farinelli, W., Laubach, H., Manstein, D., Yaroslavsky, A. N., Gubeli III, J., Jordan, K., Neil, G. R., Shinn, M., Chandler, W., et al., "Selective photothermolysis of lipid-rich tissues: A free electron laser study," *Lasers in Surgery and Medicine: The Official Journal of the American Society for Laser Medicine and Surgery* **38**(10), 913–919 (2006).

[26] Tuchin, V., "Tissue optics and photonics: Light-tissue interaction ii," *J. Biomed. Photonics Eng* **2**(3), 030201 (2016).

[27] Jacques, S. L., "Optical properties of biological tissues: a review," *Physics in Medicine & Biology* **58**(11), R37 (2013).

[28] Jacques, S. L., "Monte carlo modeling of light transport in tissue (steady state and time of flight)," in [*Optical-thermal response of laser-irradiated tissue*], 109–144, Springer (2010).

[29] Steve L. Jacques, T. L. and Prahl, S., "Monte carlo simulations of light transport in 3d heterogenous tissues (mcxyz.c)," (2013).

[30] Jacobs, J. and Love, S., "Qualitative and quantitative morphology of human sural nerve at different ages," *Brain* **108**(4), 897–924 (1985).

[31] Nachabé, R., van der Hoorn, J. W., van de Molengraaf, R., Lamerichs, R., Pikkemaat, J., Sio, C. F., Hendriks, B. H., and Sterenborg, H. J., "Validation of interventional fiber optic spectroscopy with mr spectroscopy, mas-nmr spectroscopy, high-performance thin-layer chromatography, and histopathology for accurate hepatic fat quantification," *Investigative Radiology* **47**(4), 209–216 (2012).

[32] Bendszus, M. and Stoll, G., "Technology insight: visualizing peripheral nerve injury using mri," *Nature Clinical Practice Neurology* **1**(1), 45–53 (2005).

[33] Carro, L. P., Hernando, M. F., Cerezal, L., Navarro, I. S., Fernandez, A. A., and Castillo, A. O., "Deep gluteal space problems: piriformis syndrome, ischiofemoral impingement and sciatic nerve release," *Muscles, Ligaments and Tendons Journal* **6**(3), 384 (2016).